The Astrophysical Journal Letters, 995:L5 (10pp), 2025 December 10 https://doi.org/10.3847/2041-8213/ae1f8e

Quasar Radiative Feedback May Suppress Galaxy Growth on Intergalactic Scales at $z = 6.3$

Yongda Zhu[1,18], Eiichi Egami[1], Xiaohui Fan[1], Fengwu Sun[2], George D. Becker[3], Christopher Cain[4], Huanqing Chen[5], Anna-Christina Eilers[6,7], Yoshinobu Fudamoto[8], Jakob M. Helton[1,9], Xiangyu Jin[1], Maria Pudoka[1], Andrew J. Bunker[10], Zheng Cai[11], Jaclyn B. Champagne[1,18], Zhiyuan Ji[1], Xiaojing Lin[11], Weizhe Liu (刘伟哲)[1,18], Hai-Xia Ma[12], Zheng Ma[1], Roberto Maiolino[13,14,15], George H. Rieke[1], Marcia J. Rieke[1], Pierluigi Rinaldi[1,16], Yang Sun[1], Wei Leong Tee[1], Feige Wang[17], Jinyi Yang[17], Minghao Yue[1,6], and Junyu Zhang[1]

[1] Steward Observatory, University of Arizona, 933 North Cherry Avenue, Tucson, AZ 85721, USA; yongdaz@arizona.edu
[2] Center for Astrophysics | Harvard & Smithsonian, 60 Garden Street, Cambridge, MA 02138, USA
[3] Department of Physics & Astronomy, University of California, Riverside, CA 92521, USA
[4] School of Earth and Space Exploration, Arizona State University, Tempe, AZ 85287-6004, USA
[5] Augustana Campus, University of Alberta, Camrose, AB T4V2R3, Canada
[6] MIT Kavli Institute for Astrophysics and Space Research, 77 Massachusetts Avenue, Cambridge, MA 02139, USA
[7] Department of Physics, Massachusetts Institute of Technology, Cambridge, MA 02139, USA
[8] Center for Frontier Science, Chiba University, 1-33 Yayoi-cho, Inage-ku, Chiba 263-8522, Japan
[9] Department of Astronomy & Astrophysics, The Pennsylvania State University, University Park, PA 16802, USA
[10] Department of Physics, University of Oxford, Denys Wilkinson Building, Keble Road, Oxford OX1 3RH, UK
[11] Department of Astronomy, Tsinghua University, Beijing 100084, People's Republic of China
[12] Division of Particle and Astrophysical Science, Nagoya University, Furo-cho, Chikusa-ku, Nagoya 464-8602, Japan
[13] Kavli Institute for Cosmology, University of Cambridge, Madingley Road, Cambridge, CB3 OHA, UK
[14] Cavendish Laboratory - Astrophysics Group, University of Cambridge, 19 JJ Thomson Avenue, Cambridge, CB3 OHE, UK
[15] Department of Physics and Astronomy, University College London, Gower Street, London WC1E 6BT, UK
[16] AURA for the European Space Agency (ESA), Space Telescope Science Institute, 3700 San Martin Drive, Baltimore, MD 21218, USA
[17] Department of Astronomy, University of Michigan, 1085 S. University Avenue, Ann Arbor, MI 48109, USA
Received 2025 August 29; revised 2025 November 6; accepted 2025 November 14; published 2025 December 3

Abstract

We present observational evidence that intense ionizing radiation from a luminous quasar suppresses nebular emission in nearby galaxies on intergalactic scales at $z = 6.3$. Using JWST/NIRCam grism spectroscopy from the Slitless Areal Pure-Parallel High-Redshift Emission survey and Emission-line galaxies and Intergalactic Gas in the Epoch of Reionization programs, we identify a moderate but statistically significant decline in [O III] λ5008 luminosity relative to the UV continuum (L_{5008}/L_{1500}) among galaxies within $\sim$7 comoving Mpc (cMpc) of the quasar J0100+2802, the most UV-luminous quasar known at this epoch ($M_{1450} = -29.26$). While L_{1500} remains roughly constant with transverse distance, L_{5008} increases significantly, suggesting suppression of very recent star formation toward the quasar. The effect persists after controlling for completeness, local density, and UV luminosity, and correlates with the projected photoionization-rate profile $\Gamma_{\rm qso}$. A weaker but directionally consistent suppression in L_{5008}/L_{1500} is also observed along the line of sight. The transverse suppression radius ($\sim$7 cMpc) implies a recent radiative episode with a cumulative duration $\sim$3.1 Myr, shorter than required for thermal photoheating to dominate and thus more naturally explained by rapid H_2 photodissociation and related radiative processes. Environmental effects alone appear insufficient to explain the signal. Our results provide direct, geometry-based constraints on large-scale quasar radiative feedback and recent quasar lifetimes.

Unified Astronomy Thesaurus concepts: Quasars (1319); High-redshift galaxies (734); Intergalactic medium (813)

1. Introduction

During the epoch of reionization, luminous quasars (or quasi-stellar objects, QSOs) serve as natural laboratories for studying the interplay between intense radiation fields and early galaxy formation (e.g., F. Wang et al. 2021; X. Fan et al. 2023; S. E. I. Bosman et al. 2024). These quasars illuminate their surroundings over intergalactic ($\sim$cMpc) scales (e.g., A.-C. Eilers et al. 2020), raising a key question: can quasar radiation directly suppress star formation and metal-line cooling in nearby galaxies, beyond what is expected from standard environmental clustering?

Reionization-era quasars could be the signposts of proto-clusters. Observationally, galaxies in dense environments, even at high redshift, exhibit accelerated evolution and more diverse properties (A. Dressler 1980; J. M. Helton et al. 2024a, 2024b; Q. Li et al. 2025b; T. Morishita et al. 2025; C. Witten et al. 2025). On average, protoclusters at $z \sim 2$–3 host more evolved, massive galaxies than the field, supporting an "environmental bias" scenario (e.g., C. C. Steidel et al. 2005; Y. Harikane et al. 2019; X. Lin et al. 2025). Galaxies at cosmic noon ($z \sim 2$–3) located in high-density regions also tend to show elevated ionizing photon production efficiency (Y. Zhu et al. 2025b, see also Q. Li et al. 2025a). At higher redshift ($z \sim 6$), prior to the launch of JWST, quasar environments were primarily studied using Lyα emitters

[18] JASPER Scholar.

(LAEs) and Lyman-break galaxies (LBGs; e.g., N. Kashikawa et al. 2007; S. Kim et al. 2009; Y. Utsumi et al. 2010; E. Bañados et al. 2013; T. Goto et al. 2017; S. Kikuta et al. 2017; C. Mazzucchelli et al. 2017; K. Ota et al. 2018; J. B. Champagne et al. 2023; M. Pudoka et al. 2024; M. Yue et al. 2025). Both tracers are sensitive to environment, but LAEs are additionally affected by radiative transfer and residual neutral hydrogen (M. Dijkstra 2017). Interestingly, several lower-redshift studies have found that LAEs either avoid overdense regions (P. J. Francis & J. Bland-Hawthorn 2004; N. Kashikawa et al. 2007; Y. Huang et al. 2022) or tend to populate lower-density environments (J. Cooke et al. 2013; J. Witstok et al. 2024, 2025). This behavior has been attributed to suppression of star formation in low-mass halos by an enhanced ultraviolet background (N. Kashikawa et al. 2007; L. R. Bruns et al. 2012; S. E. I. Bosman et al. 2020) and to modifications in the circumgalactic medium (CGM) structure in dense environments where the CGM is truncated or stripped (J. H. Yoon & M. E. Putman 2013).

The launch of JWST (J. P. Gardner et al. 2006), and particularly the NIRCam (M. J. Rieke et al. 2023) grism mode (e.g., T. P. Greene et al. 2017; F. Sun et al. 2023), enables a robust alternative for measuring galaxy density via rest-frame optical emission lines, especially [O III] λ5008, which is largely immune to Lyα radiative transfer effects (e.g., D. E. Osterbrock & G. J. Ferland 2006; J. M. Helton et al. 2024; X. Jin et al. 2024; J. B. Champagne et al. 2025a, 2025b; Y. Fudamoto et al. 2025; M. A. Stone et al. 2025). Radiation-hydrodynamic simulations of massive halos at $z \sim 6$–7 predict significant impacts on nearby galaxy populations via quasar winds and radiation (Y. Ni et al. 2018; T. Costa et al. 2019; J.-h. Kim et al. 2019). On larger scales, cosmological radiative transfer simulations quantify quasar radiative feedback and show that intense proximity-zone illumination can suppress star formation in small halos out to $\sim$10 cMpc by photodissociating molecular hydrogen (H_2) and heating the gas (H. Chen 2020).

In this Letter, we investigate whether high-redshift quasars can suppress star formation in neighboring galaxies through radiative feedback beyond their host halos, using a rest-frame optical tracer for the first time. We focus on J0100+2802 (X.-B. Wu et al. 2015) at $z = 6.3$ ($M_{1450} = -29.26$), the most UV-luminous quasar known at $z > 6$. This quasar hosts a large Lyα proximity zone and lies within a large-scale overdensity traced by LBGs and LAEs (e.g., A.-C. Eilers et al. 2017; M. Pudoka et al. 2024; S. Hashemi et al. 2025). Using deep JWST/NIRCam imaging and grism spectroscopy from the Slitless Areal Pure-Parallel High-Redshift Emission Survey (SAPPHIRES; F. Sun et al. 2025) and Emission-line galaxies and Intergalactic Gas in the Epoch of Reionization (EIGER; D. Kashino et al. 2023) surveys, we identify [O III]-emitting galaxies within approximately 20 cMpc of the quasar.

The remainder of this Letter is organized as follows: Section 2 describes the observations; Section 3 presents the main results and tests; Section 4 discusses implications for quasar radiative feedback and lifetimes; Section 5 concludes. Throughout this Letter, we adopt the `Planck18` cosmology (Planck Collaboration et al. 2020) and quote comoving distances unless otherwise noted.

2. Observations and Analysis

2.1. JWST Imaging and Spectroscopy

We use deep JWST/NIRCam imaging and grism spectroscopy of the $z = 6.3$ quasar J0100+2802 from the SAPPHIRES program (PID 6434; PI: E. Egami) and the EIGER survey (PID 1243; PI: S. J. Lilly).[19] J0100+2802 is among the most UV-luminous quasars known at $z > 6$ ($M_{1450} = -29.26$; X.-B. Wu et al. 2015), making it an ideal target for investigating radiative feedback on intergalactic scales. The SAPPHIRES observations were obtained in parallel to a NIRSpec (P. Jakobsen et al. 2022) multiobject spectroscopy (P. Ferruit et al. 2022) observation from program 4713 (PI: A.-C. Eilers) and consist of two overlapping NIRCam WFSS tiles. Each tile includes three dithered integrations with the GRISMR grism and F356W filter (paired with F200W for direct imaging), totaling 13,335 s per tile. These were followed by three dithered exposures in direct imaging mode using F115W and F356W (CLEAR), also totaling 13,335 s per tile. The combined on-source exposure time is 7.4 hr per filter and mode, including F356W/GRISMR, F356W imaging, F200W, and F115W. EIGER observations centered on the quasar (see D. Kashino et al. 2023) were independently reprocessed and included in our analysis to increase the effective survey area and enable direct comparisons between quasar environments. In EIGER, the nominal exposure time in a single tile (visit) is 4380 s per filter for the short-wavelength (SW) imaging and 8760 s for the WFSS.

We reduced all imaging data using a custom pipeline based on the JWST Calibration Pipeline (v1.11.3), with additional corrections for instrumental artifacts, including $1/f$ noise and snowballs. WFSS reductions were performed using the open-source pipeline from F. Sun et al. (2023),[20] with updated F356W trace and wavelength calibrations (see F. Sun et al. 2025). For each exposure, we generated 2D dispersed spectra for all cataloged sources, accounting for geometric distortion and spectral tilt, interpolated them onto a common wavelength-spatial grid, and stacked. One-dimensional spectra were extracted with a fixed 5 pixel (0.″3) boxcar. Background and continuum were removed locally using median-filter windows. Emission-line candidates were identified by visual inspection and confirmed by the [O III] $\lambda\lambda$4960, 5008 doublet: the λ5008 line must be detected at $\geqslant 5\sigma$ with a corresponding λ4960 detection at $\geqslant 2\sigma$ at the expected separation. Redshifts were measured from [O III] λ5008.

We define three redshift subsamples within the J0100 field: a proximity sample within $|\Delta z| \lesssim 0.07$ of the quasar redshift ($z \approx 6.3$), a *foreground* control at $z \approx 6.2$ (about 60 cMpc toward lower redshift), and a *background* control at $z \approx 6.8$ (about 170 cMpc toward higher redshift). Because the observed [O III] lines fall within a narrow wavelength range in F356W over $z \approx 6.2$–6.8, the depth across the three slices is very similar. After quality cuts and artifact removal, the final catalog contains 24 galaxies in the foreground sample, 22 near $z \approx 6.3$, and 17 in the background sample, out of 130 emitters over $5.3 < z < 6.9$. Figure 1 shows the SAPPHIRES and EIGER footprints with the detected [O III] emitters in each slice. We note that the galaxies near the quasar are not azimuthally uniform on the sky, with most located to the south.

[19] All the JWST data used in this paper can be found in MAST at doi:10.17909/qef7-vp09.

[20] https://github.com/fengwusun/nircam_grism

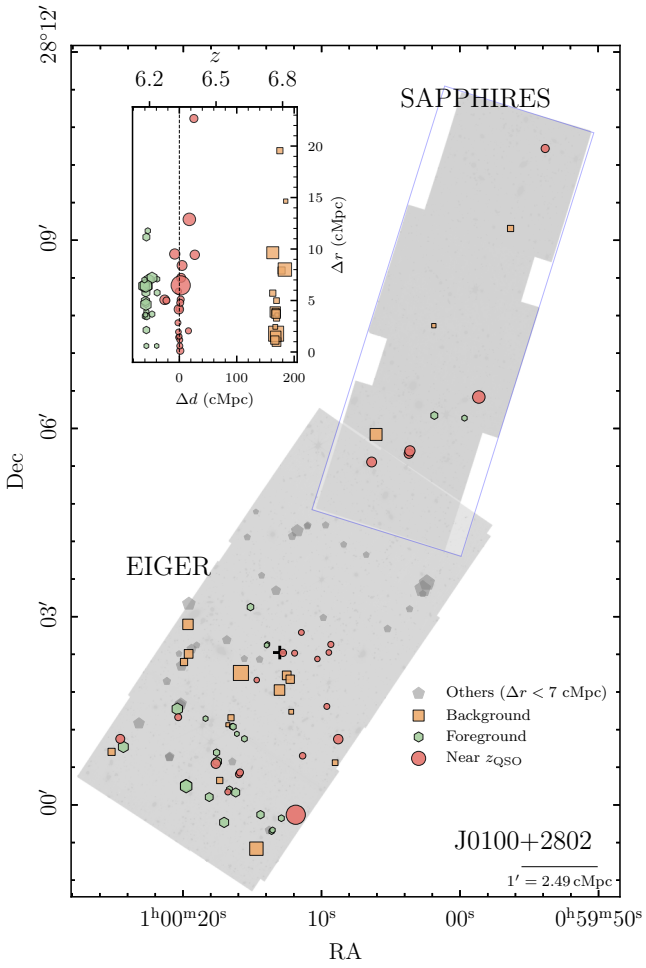

Figure 1. Sky map of the J0100+2802 field, combining NIRCam F356W mosaics from SAPPHIRES (top) and EIGER (bottom). Galaxies at $z \approx 6.3$ (near the quasar redshift; red circles), $z \approx 6.2$ (foreground; green hexagon), and $z \approx 6.8$ (background overdensity; orange squares) are shown with symbol sizes scaled by their observed [O III] λ5008 luminosities. The black cross marks the quasar position. We also show other galaxies with transverse distance from the quasar $\Delta r < 7$ cMpc on the sky map just for reference. The inset shows the projected distribution along the line of sight, with transverse separation Δr plotted against line-of-sight distance Δd from the quasar.

The two-dimensional completeness map of the EIGER mosaics (D. Kashino et al. 2025) shows nearly symmetric sensitivity across the field, and a similar excess of [O III] emitters to the south is also seen in previous analyses of the J0100 field (D. Kashino et al. 2023, 2025). This suggests that the observed anisotropy likely reflects genuine large-scale structure or cosmic variance rather than an observational bias.

2.2. Derived Quantities

[O III] λ5008 emission-line fluxes were measured from the one-dimensional, continuum-subtracted spectra by fitting a single Gaussian profile and integrating the model. Typical uncertainties on [O III] fluxes are approximately 4% based on propagated fitting errors. Rest-frame UV continuum luminosities (L_{1500}) were estimated from F115W photometry, assuming a flat f_ν spectrum. All fluxes were measured within a circular aperture of radius 0.″15, matching the spectral extraction aperture, using the `sep` package (K. Barbary 2016). We define the ratio $\log_{10}(L_{5008}/L_{1500})$ as a proxy for the ionized-gas cooling efficiency normalized by star formation rate (see the Appendix for results based on $\log_{10}(L_{5008})$). Uncertainties on this ratio are dominated by the [O III] flux error; the contribution from F115W photometric uncertainty is negligible.

To interpret the observed trends in [O III]/UV ratios in the context of quasar radiative feedback, we model the local ionizing radiation field using a physically motivated prescription for the quasar photoionization rate $\Gamma_{\rm qso}(r)$. Rather than assuming pure geometric dilution, we follow the formalism developed by G. D. Becker et al. (2021) and implemented in Y. Zhu et al. (2023), in which attenuation of Lyman-continuum (LyC) photons by the intergalactic medium (IGM) is included via a locally modified opacity $\kappa_{\rm LL}(r)$. This relation is based on stacked rest-UV spectroscopic observations of bright high-z quasars from ground-based telescopes (see also J. X. Prochaska et al. 2009; A. P. Calverley et al. 2011). The opacity is parameterized as a function of total ionizing flux as

$$\kappa_{\rm LL}(r) = \kappa_{\rm LL}^{\rm bg}\left[1 + \frac{\Gamma_{\rm qso}(r)}{\Gamma_{\rm bg}}\right]^{-\xi}, \quad (1)$$

where $\Gamma_{\rm bg}$ is the background photoionization rate and $\xi \approx 0.67$ is the power-law index describing how LyC opacity scales with the radiation field intensity (see discussions on ξ in G. D. Becker et al. 2021 and Y. Zhu et al. 2023). This model captures the reduced opacity within the quasar proximity zone due to enhanced ionizing flux.

To compute $\Gamma_{\rm qso}(r)$, we adopt an ionizing spectral energy distribution (SED) with a power-law index of $\alpha_\nu^{\rm ion} = 1.5$ and normalize the quasar luminosity at 1450 Å to its observed M_{1450}. We then calculate the ionizing luminosity at 912 Å, L_{912}, assuming a broken power-law SED with $\alpha_\nu^{\rm UV} = 0.6$ for $\lambda > 912$ Å (see G. D. Becker et al. 2021 and references therein). The geometrically attenuated profile of $\Gamma_{\rm qso}(r)$ is computed iteratively in radial steps δr, starting with

$$\Gamma_{\rm qso}(\delta r) = \Gamma_{\rm bg}\left(\frac{\delta r}{R_{\rm eq}}\right)^{-2}, \quad (2)$$

and propagating outward via

$$\Gamma_{\rm qso}(r + \delta r) = \Gamma_{\rm qso}(r)\left(\frac{r + \delta r}{r}\right)^{-2} e^{-\kappa_{\rm LL}(r)\,\delta r}, \quad (3)$$

where $R_{\rm eq}$ is the characteristic distance at which $\Gamma_{\rm qso} = \Gamma_{\rm bg}$ in the absence of attenuation, given by

$$R_{\rm eq} = \left[\frac{L_{912}\,\sigma_0}{8\pi^2\hbar\Gamma_{\rm bg}(\alpha_\nu^{\rm ion} + 2.75)}\right]^{1/2}, \quad (4)$$

as defined in A. P. Calverley et al. (2011). Here, σ_0 is the hydrogen ionization cross section at 912 Å, $\hbar$ is the reduced Planck constant, and $\alpha_\nu^{\rm ion}$ is the spectral slope of the quasar ionizing continuum (for $\lambda < 912$ Å) in the frequency domain. We adopt $\Gamma_{\rm bg} = 2 \times 10^{-13}\,{\rm s}^{-1}$ at $z = 6.3$, based on recent constraints from P. Gaikwad et al. (2023; see also F. B. Davies et al. 2023). This model enables a more accurate representation of quasar radiation profiles on intergalactic scales, which we compare to observed trends in [O III]/UV ratios as a function of distance.

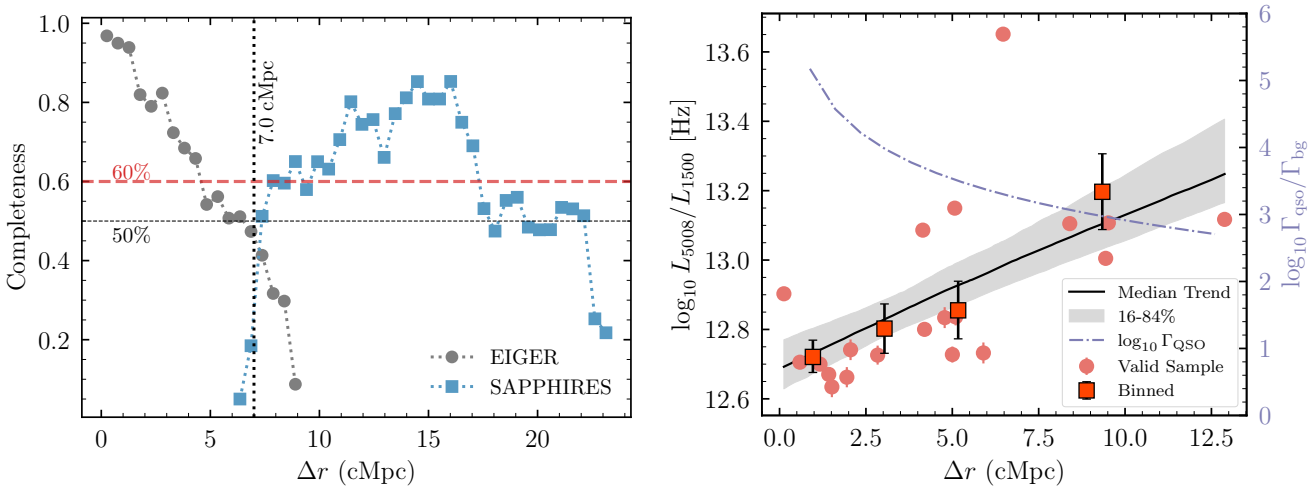

Figure 2. Left: field-averaged detection completeness for galaxies with $L_{5008} > 10^{42}$ erg s^{-1} as a function of projected transverse distance Δr (cMpc) from J0100 +2802, for the SAPPHIRES (blue squares) and EIGER (gray circles) mosaics. The horizontal dashed lines mark 50% and 60% completeness. The vertical dotted line at $\Delta r = 7$ cMpc indicates where both fields reach $\gtrsim$50% completeness (from injection-recovery tests). Right: [O III]-to-UV luminosity ratio ($\log_{10}(L_{5008}/L_{1500})$) versus Δr for galaxies that pass the Δr-dependent completeness cut (>50%; red points). The solid black line is the best-fit linear trend derived from the *unbinned data points*, and the shaded band shows the 16th to 84th percentile bootstrap interval from mock downsampling to uniform 60% completeness. Binned averages (five galaxies per bin) are shown as red squares with error bars, which represent 1σ uncertainties in the mean within each bin. The dotted–dashed purple curve shows the expected quasar photoionization rate, and the right-hand axis gives $\log_{10}(\Gamma_{QSO}/\Gamma_{bg})$.

Finally, we assess the detection completeness of [O III] sources as a joint function of L_{5008} and transverse distance from the quasar. We inject synthetic line emitters into the three-dimensional error cubes over a grid in redshift and sky position, assuming a fixed line width of 350 km s^{-1} and a range of line fluxes, and recover them with the same pipeline (see Y. Zhu et al. 2025a). The resulting completeness map for the J0100 field is consistent with D. Kashino et al. (2025). Completeness is computed as a function of L_{5008} and sky position and then averaged in bins of transverse distance from the quasar Δr. We adopt $L_{5008} > 10^{42}$ erg s^{-1} as a detection threshold, for which completeness is at least 40% in both the EIGER and SAPPHIRES fields. For the science analyses, we further require >50% completeness within each radial bin, and for bootstrap tests, we downsample to a uniform 60% completeness. Only galaxies in regions meeting these criteria are included in the trend analyses and regression fits; in the $z \approx 6.3$ sample, 20 of 22 sources pass these cuts. Raising the local completeness requirement to 75% yields the same qualitative suppression in L_{5008}.

3. Results and Discussion

3.1. Suppression with Transverse Distance

Figure 2 (left) shows the field-averaged detection completeness for galaxies with $L_{5008} > 10^{42}$ erg s^{-1} as a function of projected transverse distance Δr from J0100+2802. Completeness peaks near the center of the EIGER mosaic, declines toward its edges, where exposure time is lower, and rises again in the overlap region near the center of the SAPPHIRES field. The vertical dotted line at $\Delta r = 7$ cMpc marks the approximate transition between the two mosaics, where both reach about 50% completeness. To assess systematics, we also perform forward modeling of the observed [O III] luminosity distribution by convolving a published [O III] luminosity function with the position-dependent completeness; results are shown in the Appendix and confirm that the measured trends are not driven by completeness gradients. Here we present the empirical completeness profiles used for the main selection and fits.

In the right panel of Figure 2, we present the central result of this study: a moderate but statistically significant decrease in $\log_{10}(L_{5008}/L_{1500})$ with decreasing projected distance from the quasar, consistent with radiative feedback that suppresses recent star formation (see Section 4). Red points indicate individual galaxies that meet a local completeness threshold of >50% at their respective Δr; only these galaxies are included in the regression analysis. Binned averages (five galaxies per bin) are shown as orange squares with error bars and are broadly consistent with the fitted trend. The error bars on the binned points represent 1σ uncertainties in the mean within each bin. The solid black line indicates the best-fit linear trend, with the shaded region representing the 16th to 84th percentile range from 500 bootstrap realizations. The fitting is performed on the unbinned data points, while the binned averages are shown only for visual reference. Each bootstrap draws a completeness-matched mock sample assuming a uniform 60% detection probability. We find a slope of $\log_{10}(L_{5008}/L_{1500})$–$\Delta r$ of $0.043^{+0.016}_{-0.008}$ and a Pearson p-value of 0.012, indicating >98% significance. Given the limited radial range probed and sky coverage, we refer to this as a *trend* over the observed scales rather than a universal relation. When the single high-ratio source at $\Delta r \sim 7$ cMpc is excluded, the fitted slope remains positive within 1σ uncertainty ($0.039^{+0.007}_{-0.009}$, $p = 0.015$), confirming that the overall trend is not driven by one outlier. For consistency with the completeness transition and the region of strongest suppression, we therefore adopt a characteristic radius of ~7 cMpc to describe the observed effect.

The dotted–dashed purple curve in Figure 2 shows the predicted photoionization rate Γ_{qso} as a function of distance from the quasar, normalized by the metagalactic ionizing background Γ_{bg}. The observed trend in $\log_{10}(L_{5008}/L_{1500})$ increases with distance from the quasar, in contrast to the declining $\Gamma_{qso}(r)$ profile. A more detailed discussion of the physical interpretation is deferred to Section 4.

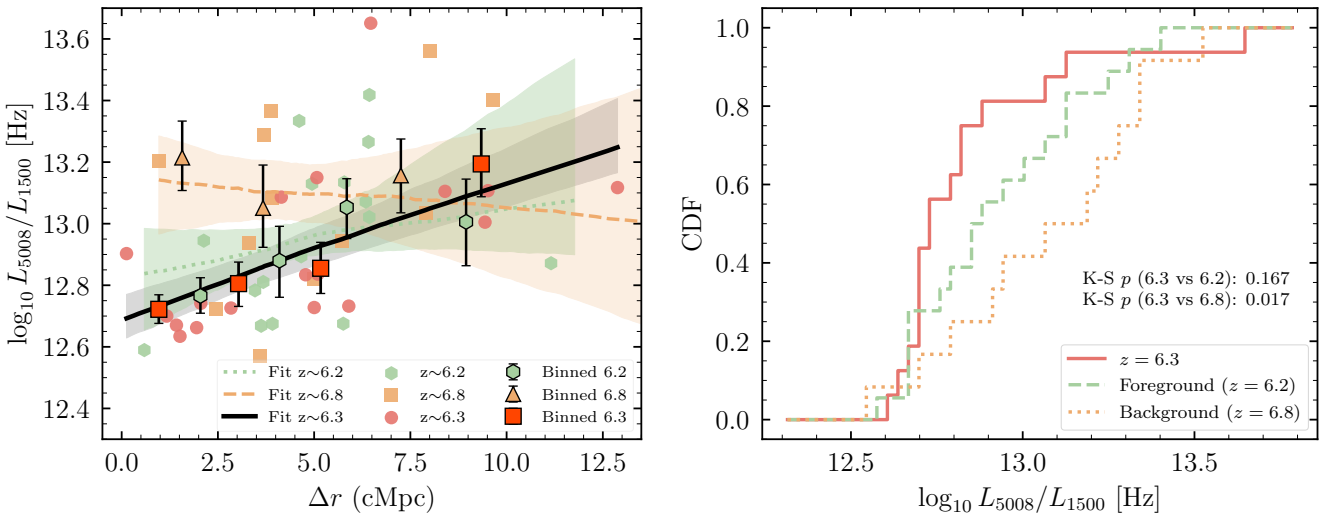

Figure 3. Left: similar to Figure 2, [O III]-to-UV ratio $\log_{10}(L_{5008}/L_{1500})$ versus transverse distance Δr for galaxies near the quasar redshift ($z \approx 6.3$, red), in the foreground ($z \approx 6.2$, green), and in the background overdensity ($z \approx 6.8$, orange). Only data points with >50% completeness are shown here. Solid, dotted, and dashed curves show completeness-matched median fits for the three slices, with shaded bands indicating the 16%–84% ranges. Binned averages (five galaxies per bin) with bootstrap uncertainties are overplotted. Right: cumulative distributions (CDFs) of $\log_{10}(L_{5008}/L_{1500})$ for galaxies within $\Delta r < 7$ cMpc of the quasar, comparing $z \approx 6.3$ (red), $z \approx 6.2$ (green), and $z \approx 6.8$ (orange). The background sample shows higher ratios than the $z \approx 6.3$ sample (K–S $p = 0.017$), while the foreground is more similar ($p = 0.167$), consistent with the visual impression from the left panel.

3.2. Line-of-Sight Trends in [O III] Luminosity

To assess whether quasar radiative feedback manifests along the line of sight (LOS), we compare galaxies at similar projected separations but offset in redshift. Figure 3 now shows both the transverse trends and the LOS comparison: the left panel plots $\log_{10}(L_{5008}/L_{1500})$ versus Δr for the near-$z_{\rm QSO}$ slice ($z \approx 6.3$; red), the foreground ($z \approx 6.2$; green), and the background overdensity ($z \approx 6.8$; orange), with completeness-matched fits and binned averages; the right panel presents cumulative distributions within $\Delta r < 7$ cMpc.

The background sample lies systematically above the $z \approx 6.3$ sequence at fixed Δr and shows only a weak slope, whereas the $z \approx 6.3$ slice exhibits the strong positive trend with distance seen in Section 3.1. Within $\Delta r < 7$ cMpc, the cumulative distribution functions (CDFs) confirm this offset: the background ratios are higher than those at $z \approx 6.3$ (Kolmogorov–Smirnov test, K–S, $p = 0.017$). By contrast, the foreground slice overlaps the $z \approx 6.3$ sample in both normalization and slope, and its CDF is statistically consistent with $z \approx 6.3$ (K–S $p = 0.167$). A similar behavior is seen for L_{5008} alone (K–S $p = 0.003$ for $z \approx 6.8$ versus $z \approx 6.3$, and $p = 0.332$ for $z \approx 6.2$ versus $z \approx 6.3$).

A natural explanation is that the $z = 6.2$ slice resides within the extended LOS proximity zone of J0100+2802, which spans tens of cMpc due to light-travel delays and the high intrinsic luminosity of the quasar (e.g., A.-C. Eilers et al. 2017). In this geometry, the LOS is effectively observed at a single quasar-on time, so a uniform suppression within the proximity zone would produce little residual correlation with LOS distance, consistent with the data. The $z \approx 6.2$ galaxies may therefore experience ionization conditions similar to those at $z \approx 6.3$.

In contrast, transverse measurements are sensitive to finite light-travel time. The significant suppression with decreasing Δr (Figure 2) implies that not all galaxies at large projected separations have yet been reached by the ionization front. This spatial anisotropy suggests a relatively recent turn-on, with an age shorter than the light-crossing time across the transverse separation, making the transverse direction a more temporally localized probe of quasar radiative feedback.

3.3. Independence from Environment and L_{1500}

To test whether the observed suppression in the [O III]-to-UV luminosity ratio is driven by environmental effects or intrinsic galaxy properties, we compare $\log_{10}(L_{5008}/L_{1500})$ against two control variables: local overdensity and UV continuum luminosity.

Figure 4 (left) shows the [O III]/UV ratio as a function of local overdensity, defined as $\log_{10}(1+\delta)$ using a $k = 5$ nearest-neighbor estimator in three-dimensional comoving space, applied to the full sample of 130 [O III] emitters ($5.3 < z < 6.9$) across both fields. The overdensity δ is normalized by the field-average number density. We caution that this is a rough estimate because peculiar velocities are unknown and the measurements cover a modest field. We find no significant correlation between $\log_{10}(L_{5008}/L_{1500})$ and $\log_{10}(1+\delta)$ for the full sample (Spearman $\rho = -0.05$, $p = 0.600$). The combined control sample (foreground $z \approx 6.2$ plus background $z \approx 6.8$; blue) shows a weak positive trend ($\rho = 0.18$, $p = 0.255$), whereas the near-$z_{\rm QSO}$ sample at $z \approx 6.3$ (red) shows a negative trend ($\rho = -0.63$, $p = 0.002$). Repeating this analysis with different k values or using kernel density estimation produces consistent results. The absence of a strong global trend with overdensity suggests that environment alone is unlikely to explain the drop in [O III]/UV near the quasar, especially since galaxies in dense regions show diverse properties, as discussed in Section 1.

In Figure 4 (right), we examine L_{1500} as a function of transverse distance Δr from J0100+2802. Both the near-$z_{\rm QSO}$ sample ($z \approx 6.3$) and the combined control sample exhibit similar $\log_{10}(L_{1500})$ distributions (K–S p-value > 0.05) with no significant radial gradient and a typical scatter of ∼0.2 dex. This confirms that the underlying UV luminosity is effectively matched across the samples.

Together, these control tests indicate that the observed decline in the [O III]/UV ratio near the quasar is not driven by

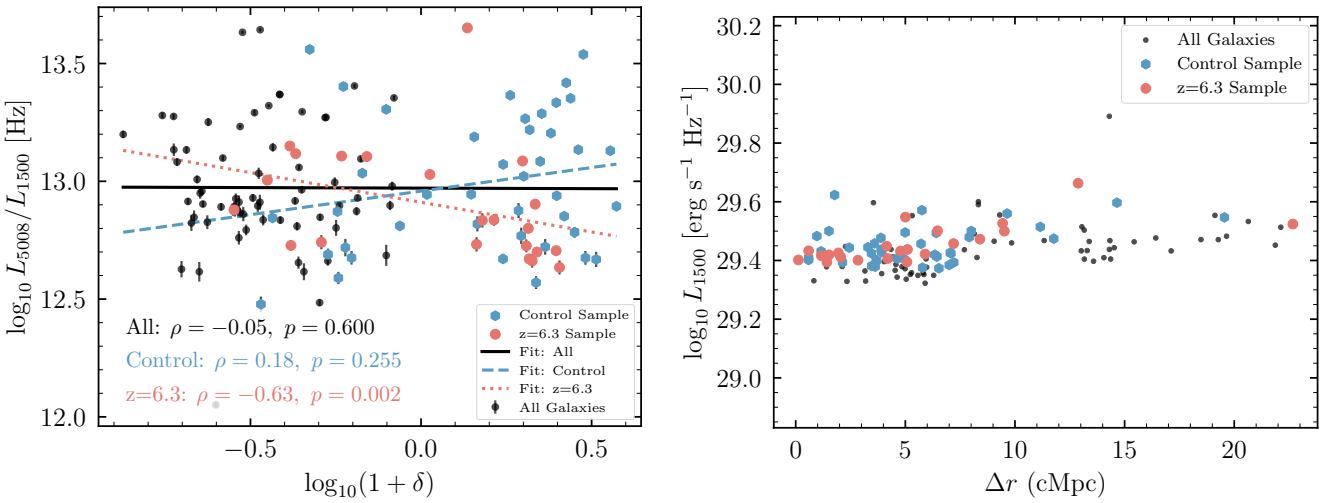

Figure 4. Left: [O III]-to-UV luminosity ratio ($\log_{10}(L_{5008}/L_{1500})$) versus local overdensity, estimated with a $k = 5$ nearest-neighbor metric in three dimensions over the full sample of 130 emitters ($5.3 < z < 6.9$) and normalized to the field average. The combined control sample (foreground $z \approx 6.2$ plus background $z \approx 6.8$; blue hexagons) shows a weak positive trend ($\rho = 0.18$, $p = 0.255$), while the $z \approx 6.3$ near-QSO sample (red circles) shows a negative trend ($\rho = -0.63$, $p = 0.002$). The full sample shows no significant correlation ($\rho = -0.05$, $p = 0.600$). These patterns indicate that the quasar-distance dependence is unlikely to be driven by local overdensity alone. Right: rest-frame UV luminosity ($\log_{10} L_{1500}$) as a function of transverse distance Δr from J0100+2802. Both the near-$z_{\rm QSO}$ and control samples show no significant trend with distance, with a typical scatter of about 0.2 dex. The y-axis span (in dex) matches Figure 2 (right) for visual comparison.

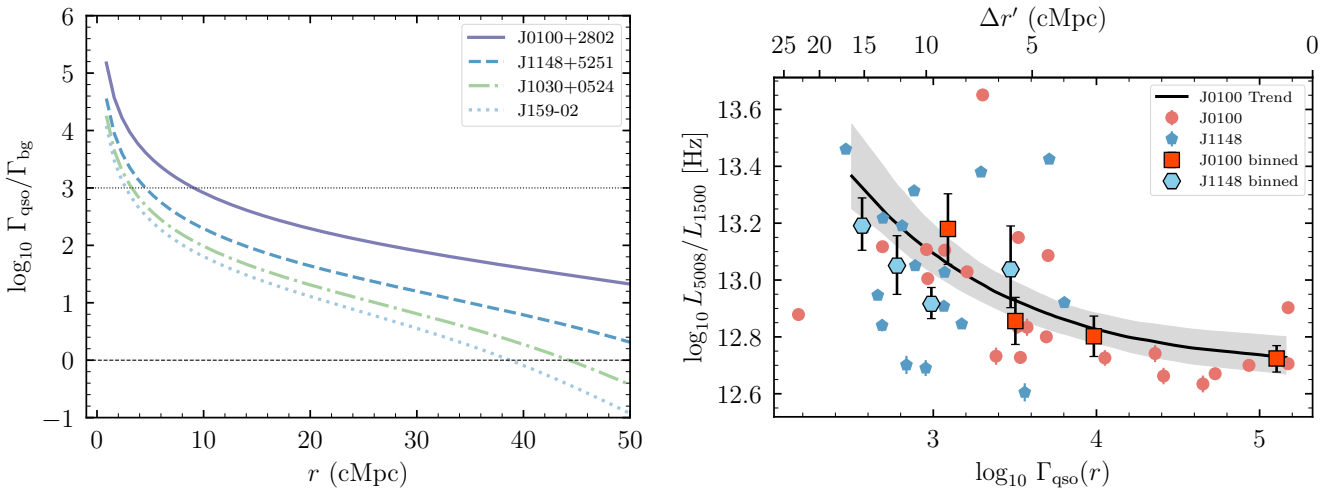

Figure 5. Left: predicted quasar photoionization rate $\Gamma_{\rm QSO}$ relative to the metagalactic UV background $\Gamma_{\rm bg}$ as a function of comoving distance r for four luminous quasars in the EIGER fields at $z \approx 6.3$. J0100+2802 (solid purple) exhibits the strongest radiative impact. The horizontal dashed and dotted lines indicate $\Gamma_{\rm QSO}/\Gamma_{\rm bg} = 1$ and 10^3. Right: [O III]-to-UV luminosity ratio $\log_{10}(L_{5008}/L_{1500})$ versus $\log_{10}\Gamma_{\rm QSO}(r)$ for galaxies near J0100+2802 (red circles) and J1148+5251 (blue pentagons). Distances for J1148 sources are rescaled to match the J0100 photoionization profile; the top axis shows the corresponding scaled transverse separation $\Delta r'$ (cMpc). The black curve and shaded band show the best-fit relation and 68% interval from the J0100 field in Figure 2 (right), replotted as a function of $\Gamma_{\rm QSO}(r)$. The J1148 data show a qualitatively similar but weaker trend, with larger scatter likely due to a smaller sample size and lower quasar luminosity. Despite this, the J1148 binned trend (cyan hexagons) is broadly consistent with the J0100 binned points (orange squares). The other EIGER quasars (J1030+0524, J159−02) lack sufficient [O III] emitters at small radii to assess this effect.

local overdensity or L_{1500} variations (see, e.g., B. Balmaverde et al. 2017; M. Pudoka et al. 2024). Instead, it primarily reflects a decline in [O III] emission and points to a distinct mechanism that selectively suppresses nebular line emission while leaving the stellar continuum relatively unaffected in the vicinity of this ultraluminous quasar.

3.4. Cross-field Comparison of [O III] Suppression and Quasar Ionizing Output

Quasar radiative feedback is expected to depend on both the ionizing luminosity of the source and the distance to surrounding galaxies. To evaluate whether the [O III] suppression observed near J0100+2802 is unique or part of a broader trend, we compare its impact with other luminous $z \approx 6.3$ quasars from the EIGER survey (D. Kashino et al. 2025), using our own uniform data reduction for consistency. The comparison sample comprises J1148+5251 ($z_{\rm qso} = 6.422$, $M_{1450} = -27.62$; E. Bañados et al. 2016; Y. Shen et al. 2019), J1030+0524 ($z_{\rm qso} = 6.304$, $M_{1450} = -26.99$; V. D'Odorico et al. 2023; C. Mazzucchelli et al. 2023), and J159–02 ($z_{\rm qso} = 6.381$, $M_{1450} = -26.47$; E. Bañados et al. 2016; E. P. Farina et al. 2022).

The left panel of Figure 5 shows the predicted quasar photoionization rate $\Gamma_{\rm qso}(r)$ normalized by the metagalactic UV background $\Gamma_{\rm bg}$ for four luminous quasars in EIGER. These profiles are computed using the attenuation-based formalism described in Section 2.2, which incorporates LyC photon absorption via a locally modified opacity (G. D. Becker

et al. 2021; Y. Zhu et al. 2023). Among the four, J0100+2802 (solid purple) exhibits the highest $\Gamma_{\rm qso}$, exceeding $\Gamma_{\rm bg}$ by over 3 orders of magnitude within $r \lesssim 7$ cMpc. This corresponds closely to the observed suppression radius in $\log_{10}(L_{5008}/L_{1500})$, where values fall below the field median. J1148+5251 (dashed blue), while less luminous ($M_{1450} \approx -27.62$), still reaches $\Gamma_{\rm qso}/\Gamma_{\rm bg} \gtrsim 10^3$ within $\sim$5 cMpc, allowing a meaningful comparison of feedback strength across quasar luminosities.

In the right panel of Figure 5, we rescale the projected transverse distance Δr for sources in the J1148+5251 field to a new variable $\Delta r'$, defined such that $\Gamma_{\rm qso,J1148}(\Delta r') = \Gamma_{\rm qso,J0100}(\Delta r)$. This enables a direct comparison of [O III]-to-UV ratios at fixed ionizing exposure across fields of differing quasar luminosity.

We find that galaxies around J1148+5251are broadly consistent with the suppression trend observed in the J0100 field, though with increased scatter. Notably, they do not show elevated $\log_{10}(L_{5008}/L_{1500})$ at fixed $\Gamma_{\rm qso}$, implying that less luminous quasars may still induce detectable feedback when $\Gamma_{\rm qso}/\Gamma_{\rm bg} \gtrsim 10^3$. In contrast, the fields around J1030+0524 and J159−02 lack bright [O III] emitters at small-scale distances ($\Delta r' \lesssim 7$ cMpc; see also D. Kashino et al. 2025), where suppression would be expected if strong feedback were present. Taken together, the scarcity of bright emitters at small-scale radii across these fields supports the interpretation that radiative suppression is genuine (see also J. B. Champagne et al. 2025a; M. Pudoka et al. 2025).

4. Interpretation and Implications

The observed decline in $\log_{10}(L_{5008}/L_{1500})$ with decreasing distance to J0100+2802, despite no corresponding trend in UV luminosity or in local galaxy density, suggests a mechanism that suppresses nebular line emission without immediately affecting the stellar continuum. The most plausible explanation is radiative feedback from the quasar acting on intergalactic scales, disrupting the ionization and cooling conditions needed for [O III] excitation while leaving the legacy of recent star formation traced by L_{1500} intact.

Radiation-hydrodynamic simulations by H. Chen (2020) show that intense quasar radiation can rapidly suppress star formation in small galaxies, especially in low-mass halos that cannot self-shield, primarily through the photodissociation of H_2. This suppression occurs within approximately 1 physical cMpc of the active galactic nucleus, with star formation rates reduced by around 0.5 dex in low-mass to average satellites, while more massive satellites remain less affected. Although line emission is not explicitly modeled, the associated delays in star formation are consistent with our finding that L_{1500} remains stable while [O III] declines near J0100. This supports a scenario in which nebular cooling and recent star formation are suppressed without erasing the established stellar population.

Meanwhile, thermal photoheating operates over much longer timescales (greater than 10^7 yr), gradually increasing the interstellar medium (ISM) thermal pressure and suppressing cold gas accretion (T. Costa et al. 2019). Proximity-zone measurements for J0100 indicate a short *recent* episode, $t_{\rm Q} \sim 10^5$ yr (A.-C. Eilers et al. 2017). This is broadly consistent with a flickering scenario in which the cumulative on-time can reach a few Myr (as implied by the transverse suppression; Section 3.1), yet it remains far shorter than the $\gtrsim 10^7$ yr required for thermal photoheating to dominate. Instead, more immediate radiative effects, such as H_2 photodissociation by Lyman–Werner photons, are more plausible. These can suppress dense-gas formation and nebular emission on short timescales while preserving the UV-bright stellar component, consistent with analytic models of abrupt ISM phase transitions triggered by critical ionizing backgrounds (A. Sternberg et al. 2014).

The transition in $\log_{10}(L_{5008}/L_{1500})$ spans nearly 1 dex in $\Gamma_{\rm qso}$, potentially indicating a nonlinear, threshold-like response rather than a smooth scaling with ionizing flux. Alternatively, the apparent jump between the 5 and 8 cMpc bins could reflect a geometric effect, such as a drop in $\Gamma_{\rm qso}$ due to shielding by a residual neutral patch. However, such structures are expected to disappear quickly given the brightness of the quasar, unless they lie outside its ionization cone. Combined with the absence of a correlation between [O III] suppression and galaxy overdensity (Figure 4), these results favor a direct radiative origin. That said, environmental mechanisms such as tidal interactions, ram pressure, or halo-related quenching could also modulate the specific star formation rate and line emission near the quasar (see Section 1). While difficult to isolate with current statistics, future surveys with larger fields and deeper spectroscopic coverage will be essential to disentangle radiative and environmental effects.

The J1148+5251 field shows a qualitatively similar but weaker trend, with $\log_{10}(L_{5008}/L_{1500})$ values that scatter both above and below the J0100 relation. This larger scatter likely reflects a combination of a smaller sample size and lower quasar luminosity. Nonetheless, the data remain consistent with mild radiative suppression when $\Gamma_{\rm qso}/\Gamma_{\rm bg} \gtrsim 10^3$, suggesting that such effects may extend to moderately luminous quasars near the end of reionization rather than being uniformly strong. Additional evidence comes from the absence of bright [O III] emitters near other luminous quasars in EIGER, particularly J1030+0524 and J159−02. These fields show a deficit of [O III] sources within scaled distances $\Delta r' \lesssim 7$ cMpc, where suppression would be expected if strong feedback were present. This could reflect either genuine feedback-induced suppression or a detection bias due to galaxies becoming too faint in [O III] (i.e., $\log_{10}(L_{5008}) < 41.6$) to be identified in current observations (see, e.g., M. A. Stone et al. 2025), possibly due to older stellar populations or low specific star formation rates. In either case, the overall pattern across multiple sightlines is consistent with a widespread but variable form of radiative influence.

Finally, the moderate but statistically significant suppression of [O III] at $\Delta r \lesssim 7$ cMpc in the J0100 field corresponds to a light-travel distance of approximately 1 proper Mpc, implying a lower bound on the quasar's radiative lifetime of about 3.1 Myr. This is significantly longer than typical estimates based on Lyα proximity-zone sizes and may indicate that the [O III] suppression reflects the integrated impact of multiple episodic bursts, with the proximity zone tracing only the most recent active phase. The presence of an extended transverse suppression region, in contrast to a compact proximity zone, supports a scenario in which the quasar flickers on timescales shorter than the timescale on which [O III] emission responds to photoionization. Because transverse distances are less affected by light-cone delays and IGM attenuation, this geometry enables a complementary and potentially more robust constraint on the cumulative radiative history of

quasars. Future work may test this scenario by searching for systematic differences in ionization-sensitive line ratios between galaxies exposed to recent versus older quasar episodes. One related caveat is that intrinsic galaxy property gradients near the quasar, for example, higher metallicity, could also weaken [O III] at fixed sSFR; targeted NIRSpec Micro-Shutter Assembly (MSA) spectroscopy of diagnostic line ratios can test this.

5. Conclusions

We present observational evidence that radiative feedback from the luminous $z = 6.3$ quasar J0100+2802 suppresses [O III] emission in nearby galaxies on intergalactic scales. Using deep JWST/NIRCam grism spectroscopy from the SAPPHIRES and EIGER programs, we find:

1. A moderate but statistically significant decline in $\log_{10}(L_{5008}/L_{1500})$ with decreasing transverse distance from the quasar, robust to variations in completeness, environment, and UV luminosity. The suppression radius of $\sim$7 cMpc implies a recent radiative burst with a minimum duration of $\sim$3.1 Myr from a light-travel time argument.
2. A weaker trend along the line of sight, consistent with extended quasar influence but less pronounced, possibly due to anisotropic emission, IGM attenuation, or light-cone effects. If confirmed with a larger sample, the transverse suppression may provide a powerful constraint on quasar lifetimes and duty cycles.
3. A comparison with other $z \sim 6.3$ quasars shows that the suppression trend near J1148+5251 is broadly consistent with that of J0100, while the deficit of bright [O III] emitters near J1030+0524 and J159−02 suggests that such suppression may be widespread. These findings imply that emission-line-selected surveys (e.g., [O III]) may underestimate galaxy densities around luminous quasars.

These results are consistent with a scenario in which quasar radiation rapidly alters ISM conditions, likely through H_2 photodissociation or ionization, suppressing recent star formation without immediately affecting the UV-bright stellar population. JWST provides direct constraints on such radiative feedback during reionization, offering a window into quasar–galaxy interaction at the highest redshifts. Future wide-field NIRCam imaging and WFSS around luminous quasars will be essential for mapping the full extent of this suppression. NIRSpec follow-up can test this scenario by searching for weak nebular lines, low ionization parameters, or older stellar populations in continuum-selected galaxies near quasars.

Acknowledgments

We thank the anonymous reviewer for the constructive feedback. Y.Z. and J.M.H. acknowledge support from the NIRCam Science Team contract to the University of Arizona, NAS5-02105. J.M.H. is also supported by JWST Program 3215. G.D.B. is supported by JWST Program 4092. Support for programs #3215, #4092, and #6434 was provided by NASA through a grant from the Space Telescope Science Institute, which is operated by the Association of Universities for Research in Astronomy, Inc., under NASA contract NAS 5-03127. H.C. thanks the support by the Natural Sciences and Engineering Research Council of Canada (NSERC), funding reference #RGPIN-2025-04798 and #DGECR-2025-00136, and by the University of Alberta, Augustana Campus. C. C. was supported by the Beus Center for Cosmic Foundations. A.J.B. acknowledges funding from the "FirstGalaxies" Advanced Grant from the European Research Council (ERC) under the European Union's Horizon 2020 research and innovation program (grant agreement No. 789056).

This work is based on observations made with the NASA/ESA/CSA James Webb Space Telescope. The data were obtained from the Mikulski Archive for Space Telescopes at the Space Telescope Science Institute, which is operated by the Association of Universities for Research in Astronomy, Inc., under NASA contract NAS 5-03127 for JWST. These observations are associated with programs #6434 and #1243. All of the data presented in this paper were obtained from the Mikulski Archive for Space Telescopes (MAST) at the Space Telescope Science Institute. The specific observations analyzed can be accessed via doi:10.17909/qef7-vp09. STScI is operated by the Association of Universities for Research in Astronomy, Inc., under NASA contract NAS5-26555. Support to MAST for these data is provided by the NASA Office of Space Science via grant NAG5–7584 and by other grants and contracts.

We respectfully acknowledge that the University of Arizona is on the land and territories of Indigenous peoples. Today, Arizona is home to 22 federally recognized tribes, with Tucson being home to the O'odham and the Yaqui. The university strives to build sustainable relationships with sovereign Native Nations and Indigenous communities through education offerings, partnerships, and community service.

This manuscript benefited from grammar checking and proofreading using ChatGPT (OpenAI 2024).

Author Contributions

Y.Z. did the analysis and wrote this paper. E.E., X.F., and F. S. contributed to the observation design. G.D.B., Y.F., J.M.H., X.J., and M.P. contributed to initial discussions and methodologies. C.C. and H.C. contributed to the theoretical interpretation. A.C.E. and M.Y. contributed to the primary observation as well as the EIGER observations. All authors contributed to discussions and interpretation of the results.

Facilities: JWST, MAST.

Software: `astropy` (Astropy Collaboration et al. 2022), `JWST Calibration Pipeline` (H. Bushouse et al. 2022).

Appendix
Robustness Tests

An important concern is whether the apparent suppression of [O III] emission near J0100+2802 could be driven by variations in survey depth across the field. In this section, we test the robustness of our result against such observational biases. Because the jump in L_{5008}/L_{1500} in Figure 2 coincides with the transition from EIGER to SAPPHIRES coverage, we restrict this test to the EIGER data and to $\Delta r < 7$ cMpc.

First, we note that the sensitivity is higher toward the field center (Figure 2). If observational bias dominated, we would expect to recover both low- and high-L_{5008}/L_{1500} galaxies close to the quasar. Instead, the opposite is observed. As shown in Figure A1(a), when selecting all galaxies within $|\Delta z| < 0.5$ of the quasar, there exists a substantial population

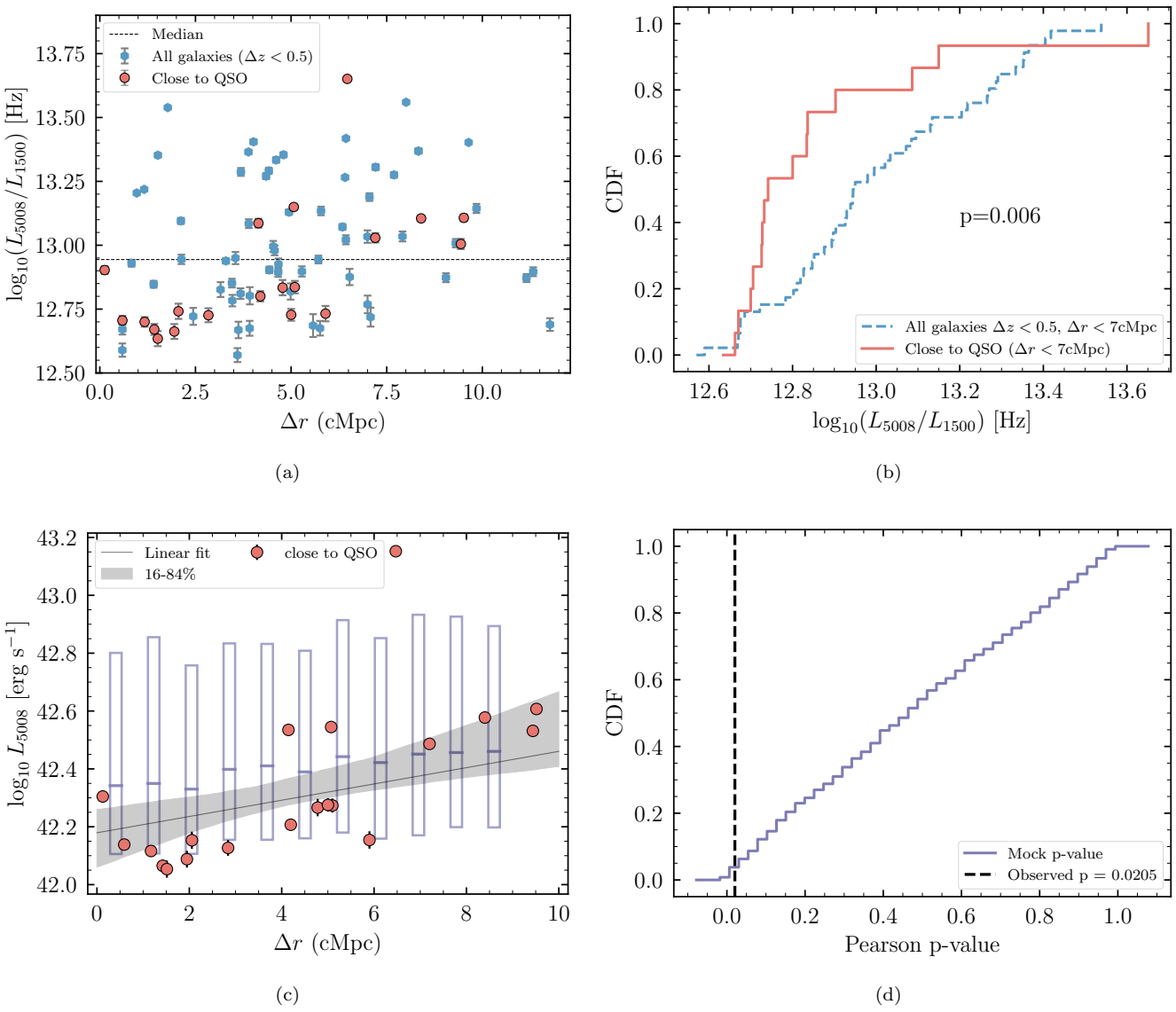

Figure A1. Robustness tests of the suppression of L_{5008} around J0100+2802. (a) $\log_{10}(L_{5008}/L_{1500})$ as a function of projected transverse distance Δr (cMpc). Red circles are galaxies near the quasar redshift; blue squares include all galaxies within $\Delta z < 0.5$ of the quasar. The horizontal dashed line marks the median of the full sample. (b) Cumulative distributions of $\log_{10}(L_{5008}/L_{1500})$ for galaxies within $\Delta r < 7$ cMpc (red: near $z_{\rm QSO}$; blue: all galaxies). A two-sample K–S test gives $p = 0.006$. (c) [O III] luminosity versus Δr for the near-$z_{\rm QSO}$ sample. The black line and gray band show the best-fit linear relation with 16%–84% bootstrap intervals. Purple boxes show the forward-modeled expectation from the J. Matthee et al. (2023) luminosity function convolved with survey completeness, plotted as per-bin medians with 16%–84% ranges (independent across bins). (d) Distribution of p-values from linear fits to 1000 mock realizations (purple CDF). The vertical dashed line marks the observed correlation ($p = 0.0205$), which lies in the ∼2% tail of the null distribution, indicating that completeness variations alone are unlikely to reproduce the observed trend.

with high L_{5008}/L_{1500} ratios. However, within $\Delta r < 7$ cMpc of the quasar (red points), this high-ratio population is absent. The cumulative distributions in Figure A1(b) further highlight this effect: the close-to-QSO sample is significantly shifted toward lower $\log_{10}(L_{5008}/L_{1500})$ compared to the rest of the galaxies within the same redshift window (blue points). A two-sample K–S test yields $p = 0.006$, confirming that the observed deficit of high L_{5008}/L_{1500} galaxies near the quasar is statistically significant ($p < 0.05$).

In the main text (Section 3), we downsampled the galaxy sample to enforce uniform completeness. Here, we carry out a more sophisticated test by explicitly forward modeling the survey selection function. We convolve the J. Matthee et al. (2023) [O III] luminosity function with the two-dimensional completeness maps as a function of source luminosity, redshift, and position, thereby accounting for both the higher central sensitivity and geometric coverage variations. The resulting mock catalogs predict the distribution of detected [O III] emitters under the null hypothesis of no environmental or quasar-induced suppression. As shown in Figure A1(c), the forward-modeled median L_{5008} values remain approximately flat with radius, with at most a weak increase (<0.2 dex) at large Δr. The distribution of slopes and p-values from 1000 mock realizations indicates that the probability of reproducing the observed positive correlation is less than 2% (Figure A1(d)).

Together, these tests demonstrate that the suppression of [O III] luminosity near J0100+2802 is unlikely to be an artifact

of varying sensitivity across the field. Instead, the deficit of bright [O III] emitters close to the quasar is likely genuine and consistent with quasar-driven radiative feedback.

ORCID iDs

Yongda Zhu https://orcid.org/0000-0003-3307-7525
Eiichi Egami https://orcid.org/0000-0003-1344-9475
Xiaohui Fan https://orcid.org/0000-0003-3310-0131
Fengwu Sun https://orcid.org/0000-0002-4622-6617
George D. Becker https://orcid.org/0000-0003-2344-263X
Christopher Cain https://orcid.org/0000-0001-9420-7384
Huanqing Chen https://orcid.org/0000-0002-3211-9642
Anna-Christina Eilers https://orcid.org/0000-0003-2895-6218
Yoshinobu Fudamoto https://orcid.org/0000-0001-7440-8832
Jakob M. Helton https://orcid.org/0000-0003-4337-6211
Xiangyu Jin https://orcid.org/0000-0002-5768-738X
Maria Pudoka https://orcid.org/0000-0003-4924-5941
Andrew J. Bunker https://orcid.org/0000-0002-8651-9879
Zheng Cai https://orcid.org/0000-0001-8467-6478
Jaclyn B. Champagne https://orcid.org/0000-0002-6184-9097
Zhiyuan Ji https://orcid.org/0000-0001-7673-2257
Xiaojing Lin https://orcid.org/0000-0001-6052-4234
Weizhe Liu (刘伟哲) https://orcid.org/0000-0003-3762-7344
Hai-Xia Ma https://orcid.org/0000-0002-5237-9433
Zheng Ma https://orcid.org/0009-0003-5402-4809
Roberto Maiolino https://orcid.org/0000-0002-4985-3819
George H. Rieke https://orcid.org/0000-0003-2303-6519
Marcia J. Rieke https://orcid.org/0000-0002-7893-6170
Pierluigi Rinaldi https://orcid.org/0000-0002-5104-8245
Yang Sun https://orcid.org/0000-0001-6561-9443
Wei Leong Tee https://orcid.org/0000-0003-0747-1780
Feige Wang https://orcid.org/0000-0002-7633-431X
Jinyi Yang https://orcid.org/0000-0001-5287-4242
Minghao Yue https://orcid.org/0000-0002-5367-8021
Junyu Zhang https://orcid.org/0000-0002-1574-2045

References

Astropy Collaboration, Price-Whelan, A. M., Lim, P. L., et al. 2022, ApJ, 935, 167
Balmaverde, B., Gilli, R., Mignoli, M., et al. 2017, A&A, 606, A23
Barbary, K. 2016, JOSS, 1, 58
Bañados, E., Venemans, B., Walter, F., et al. 2013, ApJ, 773, 178
Bañados, E., Venemans, B. P., Decarli, R., et al. 2016, ApJS, 227, 11
Becker, G. D., D'Aloisio, A., Christenson, H. M., et al. 2021, MNRAS, 508, 1853
Bosman, S. E. I., Álvarez Márquez, J., Colina, L., et al. 2024, NatAs, 8, 1054
Bosman, S. E. I., Kakiichi, K., Meyer, R. A., et al. 2020, ApJ, 896, 49
Bruns, L. R., Wyithe, J. S. B., Bland-Hawthorn, J., & Dijkstra, M. 2012, MNRAS, 421, 2543
Bushouse, H., Eisenhamer, J., Dencheva, N., et al. 2022, JWST Calibration Pipeline, v1.8.2, Zenodo, doi:10.5281/zenodo.7229890
Calverley, A. P., Becker, G. D., Haehnelt, M. G., & Bolton, J. S. 2011, MNRAS, 412, 2543
Champagne, J. B., Casey, C. M., Finkelstein, S. L., et al. 2023, ApJ, 952, 99
Champagne, J. B., Wang, F., Yang, J., et al. 2025a, ApJ, 981, 114
Champagne, J. B., Wang, F., Zhang, H., et al. 2025b, ApJ, 981, 113
Chen, H. 2020, ApJ, 893, 165
Cooke, J., Omori, Y., & Ryan-Weber, E. V. 2013, MNRAS, 433, 2122
Costa, T., Rosdahl, J., & Kimm, T. 2019, MNRAS, 489, 5181
Davies, F. B., Bosman, S. E. I., Gaikwad, P., et al. 2023, ApJ, 965, 134
Dijkstra, M. 2017, arXiv:1704.03416
D'Odorico, V., Bañados, E., Becker, G. D., et al. 2023, MNRAS, 523, 1399
Dressler, A. 1980, ApJ, 236, 351
Eilers, A.-C., Davies, F. B., Hennawi, J. F., et al. 2017, ApJ, 840, 24
Eilers, A.-C., Hennawi, J. F., Decarli, R., et al. 2020, ApJ, 900, 37
Fan, X., Bañados, E., & Simcoe, R. A. 2023, ARA&A, 61, 373
Farina, E. P., Schindler, J.-T., Walter, F., et al. 2022, ApJ, 941, 106
Ferruit, P., Jakobsen, P., Giardino, G., et al. 2022, A&A, 661, A81
Francis, P. J., & Bland-Hawthorn, J. 2004, MNRAS, 353, 301
Fudamoto, Y., Helton, J. M., Lin, X., et al. 2025, arXiv:2503.15597
Gaikwad, P., Haehnelt, M. G., Davies, F. B., et al. 2023, MNRAS, 525 4093
Gardner, J. P., Mather, J. C., Clampin, M., et al. 2006, SSRv, 123, 485
Goto, T., Utsumi, Y., Kikuta, S., et al. 2017, MNRAS, 470, L117
Greene, T. P., Kelly, D. M., Stansberry, J., et al. 2017, JATIS, 3, 035001
Harikane, Y., Ouchi, M., Ono, Y., et al. 2019, ApJ, 883, 142
Hashemi, S., Becker, G. D., Zhu, Y., & Hong, H. 2025, MNRAS, 542, 104
Helton, J. M., Sun, F., Woodrum, C., et al. 2024, ApJ, 962, 124
Helton, J. M., Sun, F., Woodrum, C., et al. 2024a, ApJ, 962, 124
Helton, J. M., Sun, F., Woodrum, C., et al. 2024b, ApJ, 974, 41
Huang, Y., Lee, K.-S., Cucciati, O., et al. 2022, ApJ, 941, 134
Jakobsen, P., Ferruit, P., Alves de Oliveira, C., et al. 2022, A&A, 661, A80
Jin, X., Yang, J., Fan, X., et al. 2024, ApJ, 976, 93
Kashikawa, N., Kitayama, T., Doi, M., et al. 2007, ApJ, 663, 765
Kashino, D., Lilly, S. J., Matthee, J., et al. 2023, ApJ, 950, 66
Kashino, D., Lilly, S. J., Matthee, J., et al. 2025, arXiv:2506.03121
Kikuta, S., Imanishi, M., Matsuoka, Y., et al. 2017, ApJ, 841, 128
Kim, J.-h., Wise, J. H., Abel, T., et al. 2019, ApJ, 887, 120
Kim, S., Stiavelli, M., Trenti, M., et al. 2009, ApJ, 695, 809
Li, Q., Conselice, C. J., Austin, D., et al. 2025a, arXiv:2508.08037
Li, Q., Conselice, C. J., Sarron, F., et al. 2025b, MNRAS, 539, 1796
Lin, X., Egami, E., Sun, F., et al. 2025, arXiv:2504.08028
Matthee, J., Mackenzie, R., Simcoe, R. A., et al. 2023, ApJ, 950, 67
Mazzucchelli, C., Bañados, E., Decarli, R., et al. 2017, ApJ, 834, 83
Mazzucchelli, C., Bischetti, M., D'Odorico, V., et al. 2023, A&A, 676, A71
Morishita, T., Liu, Z., Stiavelli, M., et al. 2025, ApJ, 982, 153
Ni, Y., Di Matteo, T., Feng, Y., Croft, R. A. C., & Tenneti, A. 2018, MNRAS, 481, 4877
OpenAI, 2024, ChatGPT-4o: Large Language Model, https://openai.com/chatgpt
Osterbrock, D. E., & Ferland, G. J. 2006, Astrophysics of Gaseous Nebulae and Active Galactic Nuclei (Univ. Science Books)
Ota, K., Venemans, B. P., Taniguchi, Y., et al. 2018, ApJ, 856, 109
Planck Collaboration, Aghanim, N., Akrami, Y., et al. 2020, A&A, 641, A6
Prochaska, J. X., Worseck, G., & O'Meara, J. M. 2009, ApJL, 705, L113
Pudoka, M., Wang, F., Fan, X., et al. 2024, ApJ, 968, 118
Pudoka, M., Wang, F., Fan, X., et al. 2025, ApJ, 987, 198
Rieke, M. J., Kelly, D. M., Misselt, K., et al. 2023, PASP, 135, 028001
Shen, Y., Wu, J., Jiang, L., et al. 2019, ApJ, 873, 35
Steidel, C. C., Adelberger, K. L., Shapley, A. E., et al. 2005, ApJ, 626, 44
Sternberg, A., Le Petit, F., Roueff, E., & Le Bourlot, J. 2014, ApJ, 790, 10
Stone, M. A., Rieke, G. H., Lyu, J., et al. 2025
Sun, F., Egami, E., Pirzkal, N., et al. 2023, ApJ, 953, 53
Sun, F., Fudamoto, Y., Lin, X., et al. 2025, arXiv:2503.15587
Utsumi, Y., Goto, T., Kashikawa, N., et al. 2010, ApJ, 721, 1680
Wang, F., Yang, J., Fan, X., et al. 2021, ApJL, 907, L1
Witstok, J., Maiolino, R., Smit, R., et al. 2025, MNRAS, 536, 27
Witstok, J., Smit, R., Saxena, A., et al. 2024, A&A, 682, A40
Witten, C., Oesch, P. A., McClymont, W., et al. 2025, arXiv:2507.06284
Wu, X.-B., Wang, F., Fan, X., et al. 2015, Natur, 518, 512
Yoon, J. H., & Putman, M. E. 2013, ApJL, 772, L29
Yue, M., Eilers, A.-C., Matthee, J., et al. 2025, ApJL, 993, L12
Zhu, Y., Becker, G. D., Christenson, H. M., et al. 2023, ApJ, 955, 115
Zhu, Y., Becker, G. D., D'Aloisio, A., et al. 2025a, arXiv:2510.09568
Zhu, Y., Bonaventura, N., Sun, Y., et al. 2025b, arXiv:2508.12599